

pubs.acs.org/NanoLett Letter

Mooij Law Violation from Nanoscale Disorder

Aifeng Wang,* Lijun Wu, Qianheng Du, Muntaser Naamneh, Walber Hugo Brito, AM Milinda Abeykoon, Wojciech Radoslaw Pudelko, Jasmin Jandke, Yu Liu, Nicholas C. Plumb, Gabriel Kotliar, Vladimir Dobrosavljevic, Milan Radovic, Yimei Zhu, and Cedomir Petrovic*



Cite This: Nano Lett. 2022, 22, 6900-6906



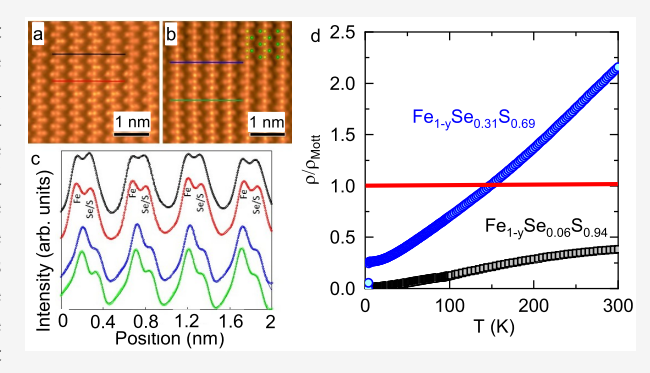
ACCESS

III Metrics & More

Article Recommendations

s Supporting Information

ABSTRACT: Nanoscale inhomogeneity can profoundly impact properties of two-dimensional van der Waals materials. Here, we reveal how sulfur substitution on the selenium atomic sites in $\operatorname{Fe}_{1-y}\operatorname{Se}_{1-x}\operatorname{S}_x$ ($0 \le x \le 1, y \le 0.1$) causes $\operatorname{Fe-Ch}$ ($\operatorname{Ch} = \operatorname{Se}, \operatorname{S}$) bond length differences and strong disorder for $0.4 \le x \le 0.8$. There, the superconducting transition temperature T_c is suppressed and disorder-related scattering is enhanced. The high-temperature metallic resistivity in the presence of strong disorder exceeds the Mott limit and provides an example of the violation of Matthiessen's rule and the Mooij law, a dominant effect when adding moderate disorder past the Drude/Matthiessen's regime in all materials. The scattering mechanism responsible for the resistivity above the Mott limit is unrelated to phonons and arises for strong $\operatorname{Se/S}$ atom disorder



in the tetrahedral surrounding of Fe. Our findings shed light on the intricate connection between the nanostructural details and the unconventional scattering mechanism, which is possibly related to charge-nematic or magnetic spin fluctuations.

KEYWORDS: disorder, defects, electrical transport, superconductivity

Atomic defects are ubiquitous in two-dimensional (2D) materials with van der Waals bonds and have the potential to significantly modulate properties and bring about useful functionalities.^{1,2} Together with interactions due to charge, orbital, spin, and lattice degrees of freedom, inhomogeneity due to nanoscale defects leaves a significant imprint on electronic and thermal transport properties.^{3,4}

The Boltzmann equation has been widely used in the past century to explain transport properties in solids.5cornerstone of the Boltzmann transport model is Matthiessen's rule, which treats all scattering processes as independent and additive. The rule is a common method in treating scattering, though discrepancies have been observed in several strongly correlated materials. 10-12 In metals, it leads to a positive resistivity slope $d\rho/dT > 0$ since thermally induced scattering increases electrical resistivity. The rule also predicts that as disorder increases so does the elastic scattering ρ_0 , whereas the temperature-dependent inelastic contribution is unaffected. This is indeed seen in many weakly disordered metals where resistivity $\rho_0 = \rho \rightarrow 0$ approaches Mott–Ioffe–Regel limit, where scattering lengths become very short and correspond to interatomic distances, leading to Anderson localization. 13-15 At strong disorder, Mooij noticed a general trend: as the metallic resistivity slope changes and eventually changes sign, the resistivity slope is inversely proportional to ρ_0 . This has been observed even at very high temperatures above the Debye temperature. 16,17

Here, we report a strong violaton of the Matthiessen's rule and Mooij law arising from nanoscale inhomogeneity of disordered Fe atomic vacancy defects and Fe-Ch (Ch = Se, S) bond distances in $\operatorname{Fe}_{1-y}\operatorname{Se}_{1-x}S_x$ ($0 \le x \le 1, y \le 0.1$), created by chemical substitution on chalcogen atomic sites in FeSe and FeS superconductors. 18,19 FeSe also features a nematic state below $T_s = 91$ K driven by charge-orbital or spin degrees of freedom, instead of the weak tetragonal-to-orthorhombic distortion of the lattice. ^{20–23} We observe a vast region for $0.4 \le x \le 0.8$ where the effects of disorder on electronic transport is strong, as seen in the dimensionless quantity $k_{\rm F}l$ < 1, where $k_{\rm F}$ is the Fermi wavenumber and $l = \nu \tau$ is the mean free path of electron wave pocket with group velocity ν and elastic scattering time τ between two successive scattering events. There, in contrast to FeSe or FeS, Fe atomic vacancies and Fe-Ch bond lengths exhibit spatial inhomogeneity on the nanoscale. In this x range, resistivity is metallic at high temperature, even though $k_{\rm F}l \sim 1$ is widely accepted to coincide with the Mott-Ioffe-Regel criterion associated with

Received: March 29, 2022 Revised: August 2, 2022 Published: August 17, 2022





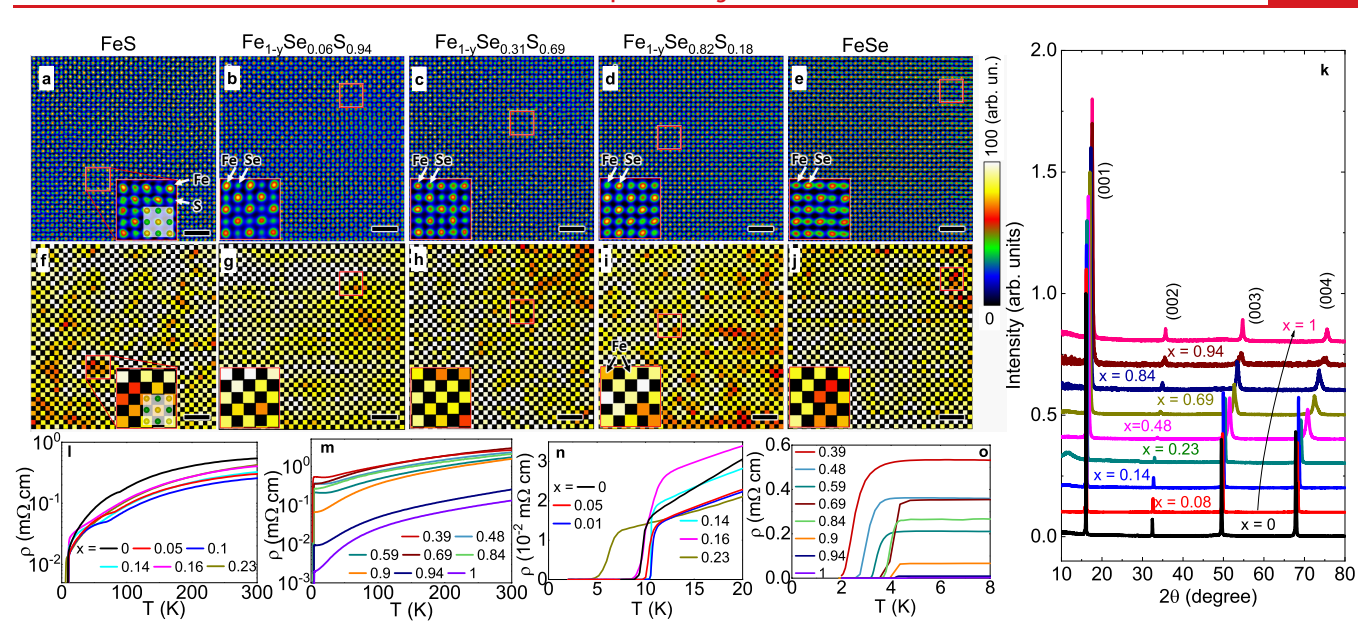


Figure 1. (a-e) STEM-HAADF images with the incident beam along the [001] direction for (a) FeS, (b) Fe_{1-y}Se_{0.06}S_{0.94}, (c) Fe_{1-y}Se_{0.31}S_{0.69}, (d) Fe_{1-y}Se_{0.82}S_{0.18}, and (e) FeSe single crystals. Scale bar 1 nm. Note that the contrast of Fe columns is stronger than that of S/Se columns in FeS, Fe_{1-y}Se_{0.06}S_{0.94}, and Fe_{1-y}Se_{0.31}S_{0.69} but becomes weaker in Fe_{1-y}Se_{0.82}S_{0.18} and FeSe. The image contrast in (d,e) is reduced to avoid displaying saturated Se/S columns. (f-j) Peak intensity map of Fe columns refined from the corresponding images in the first row. Each square represents a Fe column. Scale bar 1 nm. The insets are the magnified images from the area marked by the red squares. The [001] projection of FeS is shown in the insets in (a,f), with yellow and green spheres representing Fe and S atoms, respectively. The map clearly shows the peak intensity variation of Fe columns, indicating that the Fe vacancies vary from column to column. (k) Single crystal XRD patterns at room temperature. Patterns are offset for clarity. (l-o) Resistivity of Fe_{1-y}Se_{1-x}S_x. (n) shows an enlarged low-temperature region for (l); (o) shows an enlarged low-temperature region for (m)

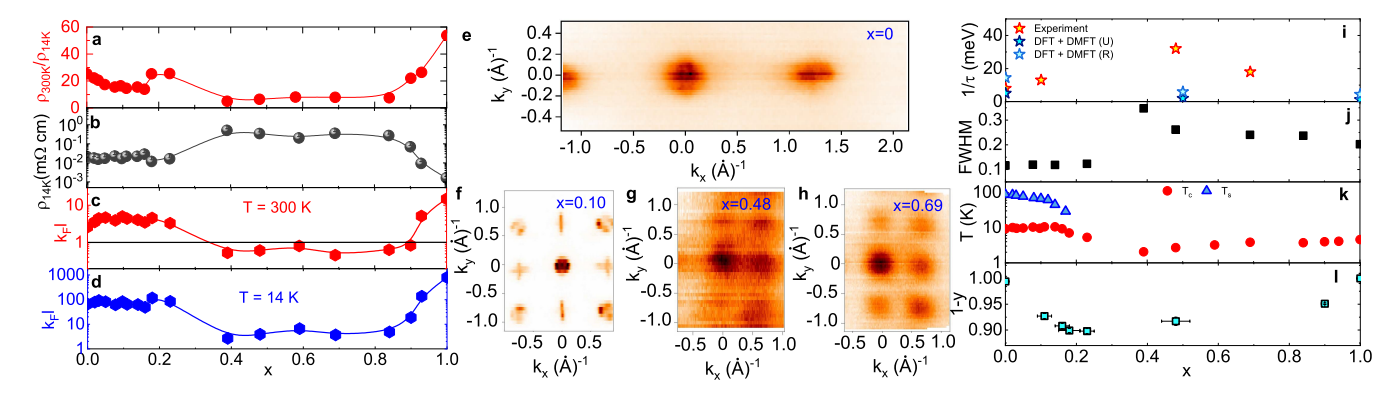


Figure 2. (a) Ratio of resistivity at 300 K to resistivity at 14 K and (b) resistivity values at 14 K. (c,d) Values of $k_F l$ for $(0 \le x \le 1)$ at 300 K and at 14 K, respectively. Fermi surface near the Γ-point in the Brillouen zone for FeSe (e), Fe_{1-y}Se_{0.9}S_{0.1} (f), Fe_{1-y}Se_{0.52}S_{0.48} (g), and Fe_{1-y}Se_{0.31}S_{0.69} (h). (i) Scattering rates at the Γ-point from experiment. Smearing of the Fermi surfaces in (e-h) gives an impression of the scattering rates, derived from the energy dispersion curves.³⁰ High 1/τ is a hallmark of disorder-related electron scattering. Note how experimental 1/τ is enhanced near x = 0.5, which is in contrast to the smooth evolution of the calculated 1/τ due to the changes in the electronic correlations. (j) fwhm of single crystal diffraction [001] peaks in Figure 1k. Larger fwhm indicates higher disorder along the crystallographic c-axis Bragg planes. (k) $T_s(x)$ and $T_c(x)$. (l) Fe stoichiometry variation with respect to x.

Anderson localization for pointlike scatterers, ²⁴ indicating the inadequacy of the Boltzmann transport model. Moreover, violation of Matthiessen's rule is inconsistent with the Mooij law, where increased disorder when electron—phonon scattering is present results in a decrease in temperature-dependent resistivity. Disorder and bad metal behavior are present in many unconventional superconductors. ^{25–27} Yet, experimental scattering rates $1/\tau$ in the bad metal state for $x \sim 0.5$ are much stronger than $1/\tau$ due to electronic correlations and in violation of Mooij's law. This implies that charge carriers might be inelastically scattered by spin fluctuations that are induced by nanoscale Fe—Ch bond disorder. ²⁸ The present

study points to the need for future studies on the role of nanoscale iron-chalcogen bond distance inhomogeneity in electron correlation tuning as well as on the charge-nematic or magnetic spin fluctuations in highly disordered S-doped FeSe where superconducting $T_{\rm c}$ shows correlation with disorder-related scattering. ^{27–29}

Unit cell refinements of X-ray diffraction (XRD) powder patterns of $\operatorname{Fe}_{1-y}\operatorname{Se}_{1-x}S_x$ ($0 \le x \le 1, y \le 0.1$) confirm phase purity.³⁰ Scanning transmission electron microscopy (STEM) images recorded by high-angle annular dark-field detector (HAADF) (Figure 1a–j) suggest the presence of nanoscale inhomogeneity and up to about 10% Fe vacancy defects that

develop for all crystals with mixed composition of Se and S on chalcogen atomic sites.³⁰ The contrast of Fe columns is stronger than that of S/Se columns in FeS, $Fe_{1-y}Se_{0.06}S_{0.94}$, and $Fe_{1-y}Se_{0.31}S_{0.69}$ but becomes weaker in $Fe_{1-y}Se_{0.82}S_{0.18}$ and FeSe. The peak intensity map shows the intensity variation of Fe and Se/S columns, indicating disordered Fe atomic vacancies. Single crystal X-ray diffraction (XRD) patterns (Figure 1k) shows (00l) reflections. The reflections shift to higher scattering angles with increasing x, consistent the decrease of the unit cell volume. The nematic transition T_s in FeSe, detected via the dip anomaly in $\rho(T)$, gradually shifts to $T_c \rightarrow 0$ as S substitutes for Se in the lattice and vanishes above x = 0.18 (Figure 1l,m); T_c increases weakly up to about 11 K for x = 0.1 (Figure 1n) which is in agreement with previous observations.^{31–34} The width of the resistivity transition around T_c broadens as x increases from 0 and T_c reaches its minimum value of 2.1 K for all $0 \le x \le 1$ at x = 0.4 (Figure 1n,o). For higher S content approaching FeS, T_c increases (Figure 10), consistent with T_c seen in $\chi(T)$.

To estimate the disorder-related scattering, we consider $\rho(300 \text{ K})/\rho(14 \text{ K})$ as the residual resistivity ratio (RRR) for all x in (Figure 11–o). In general, smaller values denote larger disorder-related scattering strength. There is a continuous decrease of RRR from x = 0 to x = 0.16 as S atoms substitute for Se and as the structural transition is suppressed (Figure 2a). When the structural/nematic transition is completely suppressed, the RRR increases to about 25. The RRR decreases with further increase in x up to x = 0.4 then shows a weak increase up to x = 0.84, and finally steeply rises to 54 at x = 1. The RRR changes with respect to x are also reflected in the residual resistivity values in the normal state close to T_{o} $\rho_{14\mathrm{K}}$ (Figure 2b). Although ρ_{14K} involves contribution of different scattering mechanisms, higher values may signal larger contributions from the disorder component. Disorder contributes to dephasing of the electronic wave function in the normal state, although for weak disorder $k_{\rm E}l \gg 1$ the superconducting T_c in an isotropic s-wave superconductor should be unaffected by nonmagnetic impurities. 17,35,36 We estimate $k_{\rm F}l$ in our samples as follows: in the Drude theory, the 2D resistivity is $\rho = (h/e^2)(d/k_{\rm F}l)$, where h is the Planck constant, e is the elementary charge, k_F is the Fermi wavenumber, d is interplane atomic distance, and l is mean free path. Approximating d by the value of the lattice parameter a at 300 K,³⁰ which changes less than 1% down to 10 K,³⁷ and using the experimental ρ values (Figure 2b),³⁰ we plot $k_{\rm F}l$ versus x in Figure 2c (300 K) and Figure 2d (14 K). T_c (Figure 1n,0) is suppressed for strong disorder.

Strong disorder (Figure 2c,d) affects angle-resolved photoemission (ARPES) electronic scattering rates $1/\tau$. There is a considerable change in the Fermi surface near the Γ point (Figure 2e-h), as seen in $1/\tau$ when x is tuned from FeSe (Figure 2e) to a weakly disordered (x = 0.1) (Figure 2f) and then strongly disordered (x = 0.48 and 0.69) (Figure 2g,h) state toward FeS. 30,38 We plot experimental scattering rates and the scattering rates due to the change in electronic correlations calculated based on a combination of dynamical mean field theory (DMFT) and density functional theory (DFT) in Figure 2i for different x. Within the DFT + DMFT framework, larger scattering rates correspond to an increase in the electronic incoherence of states near the Fermi energy. This indicates that scattering rates due to solely local electronic correlations are reduced by increasing x in $Fe_{1-y}Se_{1-x}S_x$. However, the calculated scattering rates are very small when

compared to ARPES scattering rates at the Γ -point. The degree of correlations within the model is governed by Fe–Se and Fe–S bond distances, yet experimental scattering rate changes cannot be explained by the decrease of electronic correlations with x.

Whereas $1/\tau$ due to electronic correlations show an expected decrease as the content of sulfur atoms is increased in the lattice at the expense of Se, 39,30 observed $1/\tau$ are much larger, in particular near the middle of the alloy series. Larger ARPES scattering rates are found in samples with smaller RRR (Figure 2a). Increased scattering rates near the middle of the xrange coincide with increased Bragg plane disorder along the caxis (Figure 2j). Although $T_s(x)$ and $T_c(x)$ ($0 \le x \le 1$) (Figure 2k) match well with that previously observed, 40 we note that complete suppression of T_s coincides with reduction of the residual resistivity ratio (RRR) at x = 0.18 (Figure 2a), that is, with weak (Figure 2d) crystallographic disorder-related scattering. 41,42 $T_{\rm c}$ is suppressed only when disorder is strong $(k_{\rm F}l \sim 1)$ just above $T_{\rm c}$ (Figure 2d) and when c-axis Bragg plane disorder is enhanced (Figure 2j). Although Fe vacancy defects are detected in all crystals by STEM-HAADF (Figure 1a−j), from synchrotron Rietveld refinement we conclude that defect content is negligible in the sample bulk for FeSe and FeS,³⁰ whereas Fe defect content increases up to about x =0.23 (Figure 21), coinciding with T_s suppression. Interestingly, increasing Fe vacancy defects in the nematic region does not significantly influence disorder effects on the electrical conductivity at low temperatures, as seen by the negligible changes in $k_{\rm F}l$ (Figure 2d).

In metals, the scattering rate $1/\tau = (1/\tau_e + 1/\tau_i)$ is the sum of elastic $1/\tau_e$ and inelastic component $1/\tau_i$. Impurities and crystallographic defects/disorder commonly contribute to elastic scattering. However, bond lengths regulate the Fe-Ch overlap and the FeCh₄ tetrahedron shape which in turn controls the crystal field levels and thus the orbital occupancies and relative mixing of Fe d_{xz} and d_{yz} orbitals.^{43,28} Se/S atom disorder may give rise to inelastic carrier scattering off chargenematic or magnetic spin fluctuations that are enhanced due to variable Fe-Se and Fe-S hybridization. 28,43-46 Evidence for Se/S atom disorder in the tetrahedral surroundings of the Fe atoms comes from STEM-HAADF images (Figure 3a,b). From the refinements (Figure 3c), we obtain that the full width at half-maximum (fwhm) values are 0.15(3) nm (Fe peak) and 0.20(5) nm (Se/S peak) for $Fe_{1-y}Se_{0.31}S_{0.69}$, and 0.19(1) nm (Fe) and 0.10(5) nm (Se/S) for $Fe_{1-y}Se_{0.06}S_{0.94}$, respectively. Hence, chalcogen atomic positions are substantially more disordered near the middle range of S substitution on Se atomic sites.

Now we turn our attention to normal state scattering at high temperature for high disorder. The temperature dependence of $\rho(T)$ for $x \ge 0.4$ (Figure 1m) might hint at the phonon-related scattering. To clarify this, we focus on the Bloch-Grüneisen (BG) phonon scattering mechanism

$$\rho(T) = \rho_0 + A \left(\frac{T}{\theta_D}\right)^n \int_0^{\theta_D/T} \frac{z^5}{(e^z - 1)(1 - e^{-z})} dz$$

Using Debye temperatures θ_D obtained from heat capacity measurements on $\mathrm{Fe_{1-y}Se_{0.52}S_{0.48}}$ and FeS , 30 we observe that the BG model provides an explanation for the resistivity at low temperatures but cannot explain the resistivity above about 150 K due to enhanced scattering above the phonon-related resistivity (Figure 4a,b). We plot the Mott resistivity ρ_{Mott} for

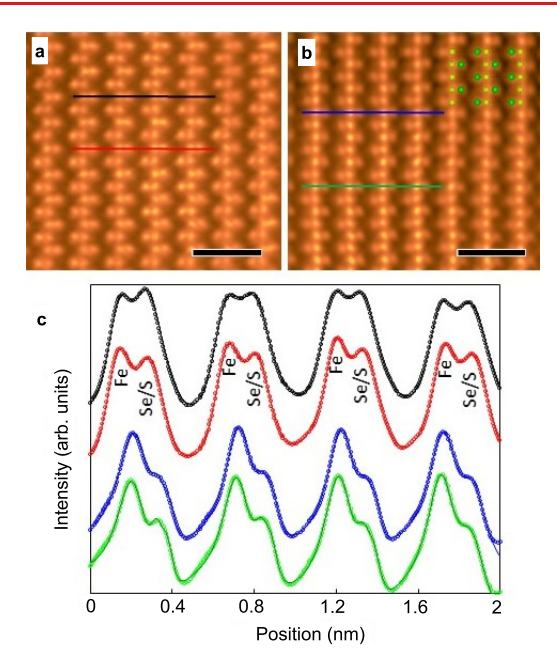


Figure 3. (a,b) STEM-HAADF images with the incident beam along the [100] direction for (a) Fe $_{1-y}$ Se $_{0.31}$ S $_{0.69}$ and (b) Fe $_{1-y}$ Se $_{0.06}$ S $_{0.94}$ single crystals. The [100] projection of the structure model is illustrated in (b) with yellow and green spheres representing Fe and Se/S atom, respectively. Scale bar 1 nm. (c) Intensity profiles (circles) from the scan lines shown in (a,b) with the corresponding colors. The solid lines are the fitted curves based on combined Gaussian and Lorentzian functions.

which $k_{\rm F}l=1$ and $\rho(T)/\rho_{\rm Mott}$ for all x in Figure 4c,d. The $\rho(T)$ curves for $(0.39 \le x \le 0.9)$ (Figure 4d) retain metallic behavior $({\rm d}\rho/{\rm d}T>0)$ at high $T\sim 300$ K, even though $k_{\rm F}l<1$, that is, the scattering rate is beyond Mott limit, suggesting an exotic scattering mechanism. ⁴⁷ Bad metal behavior with nearly linear-in-temperature resistivity is a hallmark of Hund's metals in the incoherent regime. ^{27,48–50}

In the small *x* regime, disorder can be screened by the strong correlations. 51 An increase in $\rho_{300\text{K}}/\rho_{14\text{K}}$ when T_{s} is suppressed with x (Figure 2a,k) points to an interplay of increased disorder and sudden absence of nematic correlations, implying that strong correlations could be intertwined with strong disorder when there is significant sulfur substitution. The prefactor A in resistivity is related to the electron-phonon coupling constant and is generally not very large, since $\lambda \approx$ (0.1–0.3) in known materials. In normal metals for $T \gg \theta_{\rm D}$ resistivity usually follows a $\rho = \rho_0 + AT$ linear temperature dependence which, extrapolated to very high temperatures, reaches the Mott limit far above melting temperature. When disorder is added, this increases ρ_0 , but when electron-phonon scattering is present A generally decreases with adding disorder and could even change sign at strong disorder where ρ_0 is of the order of the Mott limit; this well documented behavior is known as the Mooij correlation.⁵² The electron-phonon scattering can push the resistivity up to the Mott limit only if the disorder is already strong so that ρ_0 is near the Mott limit itself, but then the temperature-dependent resistivity term is commonly smaller when compared to the case without disorder.

Our observations are inconsistent with the Mooij scenario. First, we note the temperature-dependent part (Figure 4a,b) - i.e. the slope A of Bloch-Grüniesen resistivity fits - is much smaller for FeS when compared to $\mathrm{Fe}_{1-\nu}\mathrm{Se}_{0.52}\mathrm{S}_{0.48}^{30}$ contrary

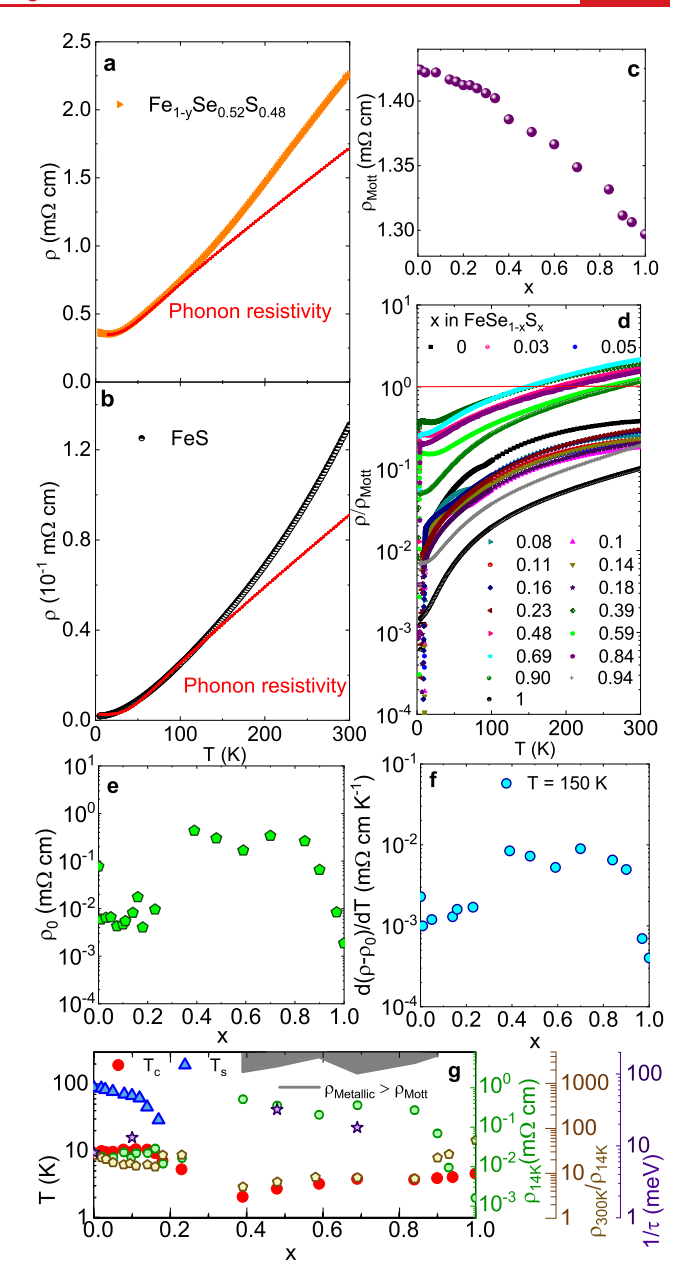


Figure 4. Data and Bloch-Grüneisen phonon scattering simulation are depicted in (a,b) using $\theta_{\rm D}=240(5)$ K for FeS and $\theta_{\rm D}=208(1)$ K for FeSe_{0.52}S_{0.48} obtained from low-temperature heat capacity fits, respectively (see text). Mott limit resistivity $\rho_{\rm Mott}(x)$ at 300 K (c), and $\rho(T)/\rho_{\rm Mott}$ for all x in Fe_{1-y}Se_{1-x}S_x (d). Red line in (d) denotes Mott limit $k_{\rm F}l=1$. (e) Residual resistivity $\rho(T\to 0)=\rho_0$. (f) Resistivity slope at 150 K. (f) Summary of experimental scattering and transport properties at Fe_{1-y}Se_{1-x}S_x (0 $\leq x \leq$ 1, $y \leq$ 0.1) phase diagram.

to Mooij scenario. See Next, let us have a look at $\rho(T)$ as x is reduced. For x=0.93 and x=1, ρ_0 is very small, and yet the high-temperature slope of $\rho(T)$ is much smaller when compared to x near the middle range of x atom substitution (Figure 4e,f), so that resistivity does not reach Mott limit at 300 K. As x is reduced from 1 in Fe_{1-y}Se_{1-x}S_x, ρ_{14K} increases more than 1 order of magnitude when compared to ρ_{14K} for FeS (Figure 2b) while temperature-dependent part of $\rho(T)$ also increases. This is unrelated to a reduction in the carrier density n. In contrast, n is increased as x is reduced from 1. See For example, already for x=0.9 the slope is much larger when

compared to x = 0.93, and as seen in the slope of $\rho(T)$, this trend continues toward the middle of the alloy series (Figure 4f).^{30,52} This is in contrast to the Mooij relation where the interplay of phonon scattering and disorder induces a slope decrease at stronger disorder. In Matthiessen's rule, $\rho(T) = \rho_0$ + $\rho_1(T)$, ρ_0 is attributed to disorder, whereas the temperaturedependent part $\rho_1(T)$ is related to various inelastic channels or correlations which are assumed independent of disorder. Increasing disorder should give an increase of ρ_0 but should not modify the slope of $\rho_1(T)$ for weak disorder, whereas for strong disorder the slope decreases and eventually changes sign.⁵² This should give a simple upward shift of the entire $\rho(T)$ curve on a linear scale, not on a logarithmic scale. Resistivity data for strong disorder indicate violation of Matthiessen's rule, contrary to Mooij's law. The fact that the x = 0.9 and x = 0.94 curves shift on a logarithmic scale indicates that increasing residual resistivity also increases temperature-dependent resistivity.

In Figure 4g, we present a summary of all transport and scattering properties. For the region of x where metallic resistivity exceeds the Mott limit at high temperature, disorder is strong (Figure 2c,d) and superconducting $T_{\rm c}$ is suppressed. The evolution of $T_{\rm c}(x)$ follows the evolution of disorder-related scattering (RRR) with x, whereas it shows inverse trend with residual resistivity just above $T_{\rm c}$ ($\rho_{\rm 14K}$) and ARPES scattering rate at the Γ -point in the Brillouen zone $1/\tau$. This points to an order parameter with nodes that gets averaged over the Fermi surface and thus reduced by scattering along with the $T_{\rm c}$.

In summary, nanoscale inhomogeneity in $Fe_{1-\nu}Se_{1-x}S_x$ (0 \leq $x \le 1$, $y \le 0.1$) results in Fe atomic vacancies and Fe-S and Fe-Se bond disorder. As x is increased and material evolves away from FeSe, there is a rise in Fe atomic vacancies and T_c is suppressed for weak disorder. Superconducting T_c in the regime of strong disorder develops on cooling from a hightemperature metallic normal state resistivity that exceeds Mott limit and violates Matthiessen's rule and the Mooij law, implying that the scattering mechanism is unrelated to phonons. This behavior is in contrast to a disorder driven metal-insulator transition where $d\rho/dT < 0$. When impurities are added to the relatively good metals FeSe and FeS, the additional scattering depends on doping in a manner that is inconsistent with the standard picture of weak disorder. We expect that our findings will stimulate further experiments and theoretical methods to connect nanoscale inhomogeneity with scattering mechanism and it is conceivable that broader distribution of Fe-chalcogen bond lengths activates chargenematic or magnetic spin fluctuations that are the dominant source of scattering for the intermediate values of x.

ASSOCIATED CONTENT

3 Supporting Information

The Supporting Information is available free of charge at https://pubs.acs.org/doi/10.1021/acs.nanolett.2c01282.

Materials synthesis and experimental methods, crystal structure, magnetic susceptibility, Bloch-Grüneisen model for $\rho(T)$ for high x, ARPES scattering rates, DFT + DMFT scattering rates, resistivity slope and carrier concentration (PDF)

AUTHOR INFORMATION

Corresponding Authors

Aifeng Wang — Condensed Matter Physics and Materials Science Department, Brookhaven National Laboratory, Upton, New York 11973, United States; Present Address: College of Physics, Chongqing University, Chongqing 401331, China; orcid.org/0000-0003-2425-3259; Email: aafwang@cqu.edu.cn

Cedomir Petrovic — Condensed Matter Physics and Materials Science Department, Brookhaven National Laboratory, Upton, New York 11973, United States; Department of Materials Science and Chemical Engineering, Stony Brook University, Stony Brook, New York 11790, United States; orcid.org/0000-0001-6063-1881; Email: petrovic@bnl.gov

Authors

Lijun Wu – Condensed Matter Physics and Materials Science Department, Brookhaven National Laboratory, Upton, New York 11973, United States

Qianheng Du — Condensed Matter Physics and Materials Science Department, Brookhaven National Laboratory, Upton, New York 11973, United States; Department of Materials Science and Chemical Engineering, Stony Brook University, Stony Brook, New York 11790, United States; Present Address: Materials Science Division, Argonne National Laboratory, Lemont, Illinois 60439, U.S.A.

Muntaser Naamneh – Department of Physics, Ben-Gurion University of the Negev, Beer-Sheva 84105, Israel

Walber Hugo Brito — Departamento de Física, Universidade Federal de Minas Gerais, 30123-970 Belo Horizonte, Minas Gerais, Brazil

AM Milinda Abeykoon — National Synchrotron Light Source II, Brookhaven National Laboratory, Upton, New York 11973, United States

Wojciech Radoslaw Pudelko – Swiss Light Source, Paul Scherrer Institut, CH-5232 Villigen, Switzerland; Physik-Institut, Universität Zürich, CH-8057 Zürich, Switzerland

Jasmin Jandke – Swiss Light Source, Paul Scherrer Institut, CH-5232 Villigen, Switzerland

Yu Liu — Condensed Matter Physics and Materials Science Department, Brookhaven National Laboratory, Upton, New York 11973, United States; Present Address: Los Alamos National Laboratory, Los Alamos, New Mexico 87545, U.S.A.; orcid.org/0000-0001-8886-2876

Nicholas C. Plumb – Swiss Light Source, Paul Scherrer Institut, CH-5232 Villigen, Switzerland

Gabriel Kotliar — Condensed Matter Physics and Materials Science Department, Brookhaven National Laboratory, Upton, New York 11973, United States; Department of Physics and Astronomy, Center for Materials Theory, Rutgers University, Piscataway, New Jersey 08854, United States

Vladimir Dobrosavljevic – Department of Physics and National High Magnetic Field Laboratory, Florida State University, Tallahassee, Florida 32306, United States

Milan Radovic – Swiss Light Source, Paul Scherrer Institut, CH-5232 Villigen, Switzerland

Yimei Zhu — Condensed Matter Physics and Materials Science Department, Brookhaven National Laboratory, Upton, New York 11973, United States; ◎ orcid.org/0000-0002-1638-7217

Complete contact information is available at: https://pubs.acs.org/10.1021/acs.nanolett.2c01282

Notes

The authors declare no competing financial interest.

ACKNOWLEDGMENTS

Work at Brookhaven National Laboratory was supported by US DOE, Office of Science, Office of Basic Energy Sciences (DOE BES), under Contract No. DE-SC0012704 (A.W., L.W., Y.L., Q.D., Y.Z. and C.P.). W.H.B. acknowledges the National Laboratory for Scientific Computing (LNCC/MCTI, Brazil) for providing HPC resources of the SDumont supercomputer, which have contributed to the research results reported within this paper. URL: http://sdumont.lncc.br. ARPES experiments were conducted at the Surface/Interface Spectroscopy (SIS) beamline of the Swiss Light Source at the Paul Scherrer Institut in Villigen, Switzerland. The authors thank the technical staff at the SIS beamline for their support. ARPES work also received support from Swiss National Science Foundation Project Nos. 200021 159678 and 200021 185037. This research used the 28-ID-1 (PDF) beamline of the National Synchrotron Light Source II, a U.S. DOE Office of Science User Facility operated for the DOE Office of Science by Brookhaven National Laboratory under Contract No. DE-SC0012704. Work in Florida (V.D.) was supported by the NSF Grant 1822258, and the National High Magnetic Field Laboratory through the NSF Cooperative Agreement No. 1644779 and the State of Florida. G.K. was supported by the US Department of energy, Office of Science, Basic Energy Sciences as a part of the Computational Materials Science Program.

REFERENCES

- (1) Liang, Q.; Zhang, Q.; Zhao, Q.; Liu, M.; Wee, A. T. S. Defect Engineering of Two-Dimensional Transition-Metal Dichalcogenides: Applications, Challenges, and Opportunities. *ACS Nano* **2021**, *15*, 2165–2181
- (2) Ryder, C. R.; Wood, J. D.; Wells, S. A.; Hersam, M. C. Chemically Tailoring Semiconducting Two-Dimensional Transition Metal Dichalcogenides and Black Phosphorus. *ACS Nano* **2016**, *10*, 3900–3917.
- (3) Zhong, J.; Stocks, G. M. Localization/Quasi-Delocalization Transitions and Quasi-Mobility-Edges in Shell-Doped Nanowires. *Nano Lett.* **2006**, *6*, 128–132.
- (4) Utterback, J. K.; Sood, A.; Cropceanu, I.; Guzelturk, B.; Talapin, D. V.; Lindenberg, A. M.; Ginsberg, N. S. Nanoscale Disorder Generates Subdiffusive Heat Transport in Self-Assembled Nanocrystal Films. *Nano Lett.* **2021**, *21*, 3540–3547.
- (5) Boltzmann, L. Lectures on Gas Theory; University of California Press: Los Angeles, 1964.
- (6) Cercignani, C. The Boltzmann Equation and Its Applications; Springer: New York, 1988.
- (7) Mertig, I. Transport properties of dillute alloys. *Rep. Prog. Phys.* **1999**, *62*, 237–276.
- (8) Aronov, A. G.; Gal'perin, Yu. M.; Gurevich, V. L.; Kozub, V. I. Weighted Monte Carlo approach to electron transport in semi-conductors. *Adv. Phys.* **1981**, *30*, 539–592.
- (9) Rossi, F.; Poli, P.; Jacobini, C. The Boltzmann-equation description of transport in superconductors. *Semicond. Sci. Technol.* **1992**, *7*, 1017–1035.
- (10) Walker, D. J. C.; Mackenzie, A. P.; Cooper, J. R. Transport properties of zinc-doped $YBa_2Cu_3O_{7-\delta}$ thin films. *Phys. Rev. B* **1995**, *51*, 15653–15656.
- (11) Prozorov, R.; Konczykowski, M.; Tanatar, M. A.; Wen, H.-H.; Fernandes, R. M.; Canfield, P. C. Interplay between superconductivity and itinerant magnetism in underdoped $Ba_{1-x}K_xFe_2As_2$ (x=0.2) probed by the response to controlled point-like disorder. *npj Quantum Materials* **2019**, *4*, 34.

- (12) Wang, Y.; Bosse, G.; Nair, H. P.; Schreiber, N. J.; Ruf, J. P.; Cheng, B.; Adamo, C.; Shai, D. E.; Lubashevsky, Y.; Schlom, D. G.; Shen, K. M.; Armitage, N. P. Subterahertz Momentum Drag and Violation of Matthiesen's Rule in an Ultraclean Ferromagnetic SrRuO₃ Metallic Thin Films. *Phys. Rev. Lett.* **2020**, *125*, 217401.
- (13) Fisk, Z.; Webb, G. W. Saturation of the high-temperture normal-state electrical resistivity of superconductors. *Phys. Rev. Lett.* **1976**, *36*, 1084–1086.
- (14) Gunnarsson, O.; Calandra, M.; Han, J. E. Colloquium: saturation of electrical resistivity. *Rev. Mod. Phys.* **2003**, *75*, 1085–1009
- (15) Anderson, P. W. Absence of diffusion in certain random lattices. *Phys. Rev.* **1958**, *109*, 1492–1505.
- (16) Mooij, J. H. Electrical conduction in concentrated disordered transition metal alloys. *J. Phys. Status Solidi* **1973**, *17*, 521.
- (17) Lee, P. A.; Ramakrishnan, T. V. Disordered electronic systems. Rev. Mod. Phys. 1985, 57, 287.
- (18) Hsu, F.-C.; Luo, J.-Y.; Yeh, K.-W.; Chen, T.-K.; Huang, T.-W.; Wu, P. M.; Lee, Y.-C.; Huang, Y.-L.; Chu, Y.-Y.; Yan, D.-C.; Wu, M.-K. Superconductivity in the PbO-type structure α -FeSe. *Proc. Natl. Acad. Sci. U.S.A.* **2008**, *105*, 14262–14264.
- (19) Lai, X.; Zhang, H.; Wang, Y.; Wang, X.; Zhang, X.; Lin, J.; Huang, F. Observation of Superconductivity in Tetragonal FeS. *J. Am. Chem. Soc.* **2015**, *137*, 10148–10151.
- (20) Chowdhury, D.; Berg, E.; Sachdev, S. Nematic order in the vicinity of a vortex in superconducting FeSe. *Phys. Rev. B* **2011**, *84*, 205113.
- (21) Baek, S-H.; Efremov, D. V.; Ok, J. M.; Kim, J. S.; van den Brink, J.; Buchner, B. Orbital-driven nematicity in FeSe. *Nat. Mater.* **2015**, *14*, 210–214.
- (22) Massat, P.; Farina, D.; Paul, I.; Karlsson, S.; Strobel, P.; Toulemonde, P.; Measson, M.-A.; Cazayous, M.; Sacuto, A.; Kasahara, S.; Shibauchi, T.; Matsuda, Y.; Gallais, Y. Charge-induced nematicity in FeSe. *Proc. Natl. Acad. Sci. U.S.A.* **2016**, *113*, 9177–9181.
- (23) Wang, F.; Kivelson, S. A.; Lee, D.-H. Nematicity and quantum paramagnetism in FeSe. *Nat. Phys.* **2015**, *11*, 959–963.
- (24) Lagendijk, A.; van Tiggelen, B.; Wiersma, D. S. Fifty years of Anderson localization. *Phys. Today* **2009**, *62*, 24–29.
- (25) Emery, V. J.; Kivelson, S. A. Superconductivity in bad metals. *Phys. Rev. Lett.* **1995**, *74*, 3253.
- (26) Haule, K.; Shim, J. H.; Kotliar, G. Correlated electronic structure of LaO_{1-x}F_xFeAs. *Phys. Rev. Lett.* **2008**, *100*, 226402.
- (27) Haule, K.; Kotliar, G. Coherence—incoherence crossover in the normal state of iron oxypnictides and importance of Hunds rule coupling. *New. J. Phys.* **2009**, *11*, 025021.
- (28) Yin, Z. P.; Haule, K.; Kotliar, G. Kinetic frustration and the nature of the magnetic and paramagnetic states in iron pnictides and iron chalcogenides. *Nat. Mater.* **2011**, *10*, 932.
- (29) Taillefer, L. Scattering and Pairing in Cuprate Superconductors. *Annu.Rev.Condens.Matter Phys.* **2010**, *1*, 51–70.
- (30) See Supporting Information.
- (31) Hosoi, S.; Matsuura, K.; Ishida, K.; Wang, H.; Mizukami, Y.; Watashige, T.; Kasahara, S.; Matsuda, Y.; Shibauchi, T. Nematic quantum critical point without magnetism in $FeSe_{1-x}S_x$ superconductors. *Proc. Natl. Acad. Sci. U. S. A.* **2016**, *113*, 8139.
- (32) Mizuguchi, Y.; Tomioka, F.; Tsuda, S.; Yamaguchi, T.; Takano, Y. Substitution Effects on FeSe Superconductor. *J. Phys. Soc. Jpn.* **2009**, *78*, 074712.
- (33) Liu, Y.; Wang, A.; Ivanovski, V. N.; Du, Q.; Koteski, V.; Petrovic, C. Thermoelectricity and electronic correlation enhancement in FeS by light Se doping. *Phys. Rev. B* **2022**, *105*, 045133.
- (34) Wang, A.; Milosavljevic, A.; Abeykoon, A. M. M.; Ivanovski, V.; Du, Q.; Baum, A.; Stavitski, E.; Liu, Y.; Lazarevic, N.; Attenkofer, K.; Hackl, R.; Popovic, Z.; Petrovic, C. Suppression of Superconductivity and Nematic Order in $\text{Fe}_{1,y}\text{Se}_{1,x}\text{S}_x$ ($0 \le x \le 1$; $y \le 0.1$) Crystals by Anion Height Disorder. *Inorg. Chem.* **2022**, *61*, 11036–11045.
- (35) Anderson, P. Absence of Diffusion in Certain Random Lattices. *Phys. Rev.* **1958**, *109*, 1492–1505.

- (36) Anderson, P. Theory of dirty superconductors. J. Phys. Chem. Solids 1959, 11, 26-30.
- (37) Margadonna, S.; Takabayashi, Y.; McDonald, M. T.; Kasperkiewicz, K.; Mizuguchi, Y.; Takano, Y.; Fitch, A. N.; Suard, E.; Prassides, K. Crystal structure of the new FeSe_{1-x} superconductor. Chem. Commun. 2008, 43, 5607.
- (38) Hoesch, M.; Gannon, L.; Shimada, K.; Parrett, B. J.; Watson, M. D.; Kim, T. K.; Zhu, X.; Petrovic, C. Disorder Quenching of the Charge Density Wave in ZrTe₃. Phys. Rev. Lett. 2019, 122, 017601.
- (39) Coldea, A. I.; Blake, S. F.; Kasahara, S.; Haghighirad, A. A.; Watson, M. D.; Knafo, W.; Choi, E. S.; McCollam, A.; Reiss, P.; Yamashita, T.; Bruma, T.; Speller, S. C.; Matsuda, Y.; Wolf, T.; Shibauchi, T.; Schofield, A. J. Evolution of the low-temperature Fermi surface of superconducting FeSe_{1-x}S_x across a nematic phase transition. NPJ. Quant. Mater. 2018, 4, eaar6419.
- (40) Yi, X.; Xing, X.; Qin, L.; Feng, J.; Li, M.; Zhang, Y.; Meng, Y.; Zhou, N.; Sun, Y.; Shi, Z. Hydrothermal synthesis and complete phase diagram of FeSe_{1-x}S_x ($0 \le x \le 1$) single crystals. Phys. Rev. B 2021, 103, 144501.
- (41) Böhmer, A. E.; Taufour, V.; Straszheim, W. E.; Wolf, T.; Canfield, P. C. Variation of transition temperatures and residual resistivity ratio in vapor-grown FeSe. Phys. Rev. B 2016, 94, 024526.
- (42) Rössler, S.; Huang, C. L.; Jiao, L.; Koz, C.; Schwarz, U.; Wirth, S. Influence of disorder on the signature of the pseudogap and multigap superconducting behavior in FeSe. Phys. Rev. B 2018, 97, 094503
- (43) Fernandes, R. M.; Chubukov, A. V.; Schmalian, J. What drives nematic order in iron-based superconductors. Nat. Phys. 2014, 10, 97.
- (44) Rømer, A. T.; Hirschfeld, P. J.; Andersen, B. M. Raising the Critical Temperature by Disorder in Unconventional Superconductors Mediated by Spin Fluctuations. Phys. Rev. Lett. 2018, 121, 027002.
- (45) Glamazda, A.; Lemmens, P.; Ok, J. M.; Kim, J. S.; Choi, K. Y. Dichotomic nature of spin and electronic fluctuations in FeSe. Phys. Rev. B 2019, 99, 075142.
- (46) Ruiz, H.; Wang, Y.; Moritz, B.; Baum, A.; Hackl, R.; Devereaux, T. P. Frustrated magnetism from local moments in FeSe. Phys. Rev. B 2019, 99, 125130.
- (47) Takagi, H.; Batlogg, B.; Kao, H. L.; Kwo, J.; Cava, R. J.; Krajewski, J. J.; Peck, W. F., Jr. Systematic Evolution of Temperature-Dependent Resistivity in La_{2-x}Sr_xCuO₄. Phys. Rev. Lett. 1992, 69, 2975-2972.
- (48) Allen, P. B.; Berger, H.; Chauvet, O.; Forro, L.; Jarlborg, T.; Junod, A.; Revaz, B.; Santi, G. Transport properties, thermodynamic properties and electronic structure of SrRuo₃. Phys. Rev. B 1996, 53, 4393.
- (49) Dang, H. T.; Mravlje, J.; Georges, A.; Millis, A. J. Electronic correlations, magnetism, and Hund's rule coupling in the ruthenium perovskites SrRuO₃ and CaRuO₃. Phys. Rev. B 2015, 91, 195149.
- (50) Deng, X.; Haule, K.; Kotliar, G. Transport Properties of Metallic Ruthenates, a DFT+DMFT Investigation. Phys. Rev. Lett. **2016**, 116, 256401.
- (51) Tanaskovic, D.; Dobrosavljevic, V.; Abrahams, E.; Kotliar, G. Disorder Screening in Strongly Correlated Systems. Phys. Rev. Lett. 2003, 91, 066603.
- (52) Ciuchi, S.; Di Sante, D.; Dobrosavljevic, V.; Fratini, S. The origin of Mooij correlations in disordered metals. NPJ. Quantum Materials 2018, 44, 3.

□ Recommended by ACS

Dynamic Observation of Topological Soliton States in a **Programmable Nanomechanical Lattice**

Shaochun Lin, Jiangfeng Du, et al.

IANIIARY 13 2021 NANO I FTTERS

READ 2

Two-Dimensional Magnets beyond the Monolayer Limit

Andrey M. Tokmachev, Vyacheslav G. Storchak, et al.

JUNE 15, 2021

ACS NANO

READ 🗹

Third-Order Optical Nonlinearity of Three-Dimensional **Massless Dirac Fermions**

J. L. Cheng, S. W. Wu, et al.

JULY 27, 2020

ACS PHOTONICS

READ **C**

Néel Vector Induced Manipulation of Valence States in the Collinear Antiferromagnet Mn₂Au

H. J. Elmers, M. Jourdan, et al.

NOVEMBER 25, 2020

ACS NANO

READ **'**

Get More Suggestions >

Supplementary Information for: Mooij Law Violation from Nanoscale Disorder

Aifeng Wang,*,†,∆ Lijun Wu,† Qianheng Du, †,‡,▽ Muntaser Naamneh,¶ Walber Hugo Brito,§ AM Milinda Abeykoon,∥ Wojciech Radoslaw Pudelko,¹ Jasmin Jandke,¹ Yu Liu,†,†† Nicholas C. Plumb,¹ Gabriel Kotliar,†,# Vladimir Dobrosavljevic,@ Milan Radovic,¹ Yimei Zhu† and Cedomir Petrovic†,‡,*

†Condensed Matter Physics and Materials Science Department, Brookhaven National Laboratory, Upton11973 New York USA

†Materials Science and Chemical Engineering Department, Stony Brook University, Stony Brook 11790 New York USA

*Department of Physics, Ben-Gurion University of the Negev, Beer-Sheva, 84105, Israel

*Departmento de Física, Universidade Federal de Minas Gerais, C. P. 702, 30123-970 Belo Horizonte, Minas Gerais, Brazil

*National Synchrotron Light Source II, Brookhaven National Laboratory, Upton, New York 11973, USA

*Swiss Light Source, Paul Scherrer Institut, CH-5232 Villigen, Switzerland

*Department of Physics and Astronomy, Center for Materials Theory, Rutgers University, Piscataway, NJ 08854 USA

*Deparatment of Physics and National High Magnetic Field Laboratory, Florida State University, Tallahassee, FL 32306 USA

1. EXPERIMENTAL METHODS

Single crystals of Fe_{1-y}Se_{1-x}S_x ($0 \le x \le 0.23$, $y \le 0.1$) were grown using an eutectic mixture of the KCl and AlCl₃ as the transport agent. ¹⁻³ Single crystals of Fe_{1-y}Se_{1-x}S_x ($0.39 \le x \le 1$, $y \le 0.1$) were synthesized by deintercalation of potassium

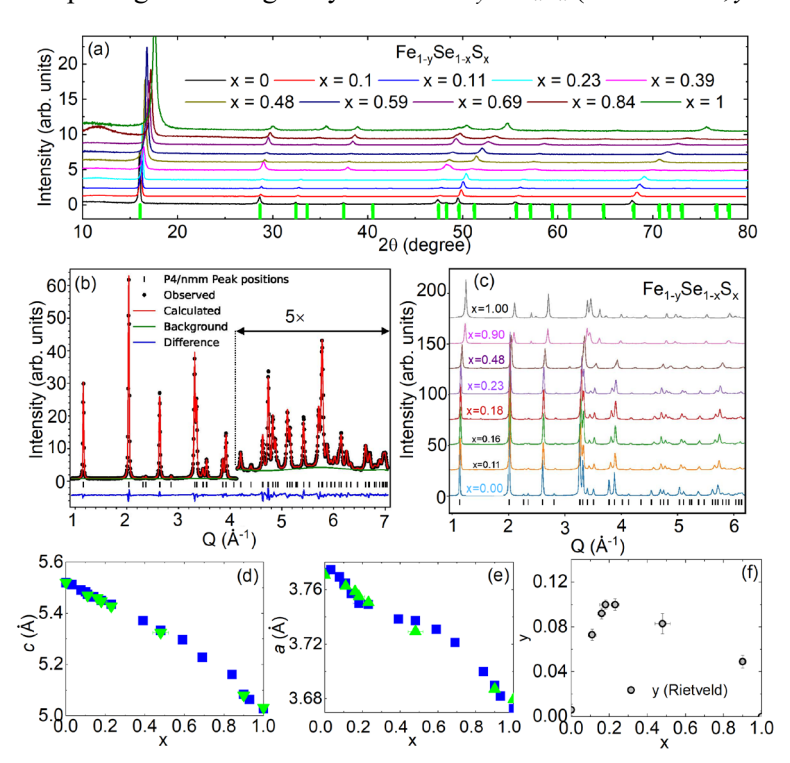


FIG. S1. Laboratory (a) and synchrotron (b,c) powder X-ray diffraction patterns. Evolution of a, c unit cell parameters (d,e) and Fe vacancy defects y (f) in Fe_{1-y}Se_{1-x}S_x ($0 \le x \le 1$) crystals from Rietveld refinement. Blue (green) symbols in (d,e) denote laboratory (synchrotron) unit cell refinement result.

from the corresponding $K_{0.8}Fe_{2-\nu}(Se_{1-x}S_x)_2$ single crystals using the hydrothermal reaction method.^{3,4} Crystal stoichiometry was determined examination of multiple points on cleaved fresh surfaces and checked by multiple samples from the batch using energy-dispersive X-ray spectroscopy in a JEOL LSM-6500 scanning electron microscope. Laboratory powder X-ray diffraction data were acquired on a Rigaku Miniflex powder diffractometer with Cu K_{α} ($\lambda = 0.15418$ nm) at room temperature. Synchrotron powder X-ray diffraction was measured on pulverized crystals using 0.0166 nm synchrotron radiation of National Synchrotron Light Source 2 at 28-ID-1 beamline. The Rietveld analysis was performed using the GSAS-II software package. 5 Magnetic susceptibility was measured in a Quantum Design MPMS-XL5. Electrical transport and heat capacity were measured in a Quantum Design PPMS-9. Hall resistivity was measured using the standard four-probe method as a difference of transverse resistance measured at positive and negative fields, i.e., ρ_{xy} ($\mu_0 H$) = $[\rho(+\mu_0 H) - \rho(-\mu_0 H)]/2$ to remove voltage probe misalignment. High-resolution scanning transmission electron microscopy (STEM) imaging were carried out using the double aberration-

^{*}To whom correspondence should be addressed: afwang@cqu.edu.cn and petrovic@bnl.gov

^ΔPresent address: College of Physics, Chongqing University, Chongqing, China.

[∇]Present address: Materials Science Division, Argonne National Laboratory, Lemont, Illinois 60439, USA

^{††}Present address: Los Alamos National Laboratory, MS K764, Los Alamos NM 87545, USA

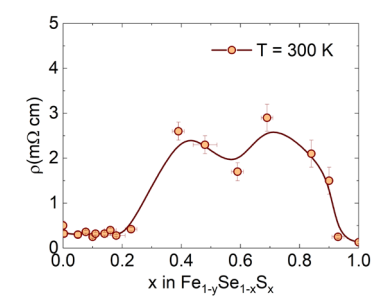


FIG. S2. Room temperature resistivity in Fe_{1-y}Se_{1-x}S_x ($0 \le x \le 1, y \le 0.1$).

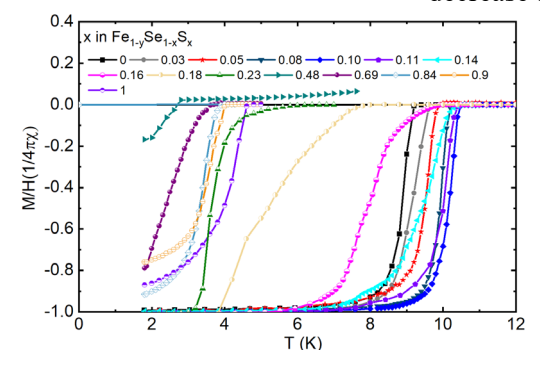


FIG. S3. M/H of Fe_{1-y}Se_{1-x}S_x ($0 \le x \le 1, y \le 0.1$).

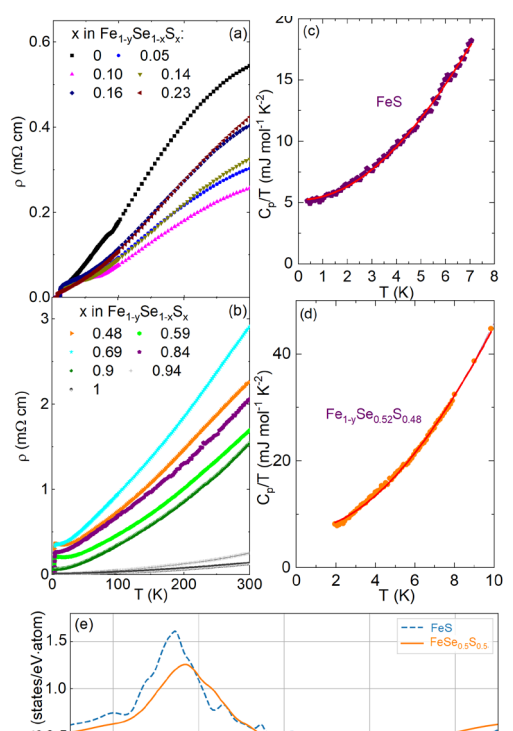


FIG. S4. Temperature dependence of resistivity for $Fe_{1-y}Se_{1-x}S_x$ for $(0 \le x \le 1, y \le 0.1)$ (a,b) and heat capacity for x = 0.48 and 1 (c,d) where line denotes a fit with Debye model. Note much larger temperature-dependent part for x = 0.9 when compared to x = 0.94. Changes in the DOS at the Fermi level in FeSe_{0.5}S_{0.5} when compared to FeS.

0.2

S0.5

corrected JEOL-ARM200CF microscope with high angle annular dark field (HAADF) detector and operated at 200 kV. The STEM-HAADF images were acquired with convergent semi angle of 21 mrad and collection semi angle from 67 to 275 mrad, respectively. The STEM samples were prepared by crushing the crystals and dispersed on a Lacy carbon TEM grid.

2. CRYSTAL STRUCTURE

No impurity was observed in either laboratory or synchrotron powder X-ray data Fig. S1a-c). The evolution of unit cell parameters a, c (Fig. S1d,e) shows gradual decrease as S replaces Se. Attempts to refine Se/S vacancy content in all crystals did

not improve fit significantly. Due to the bulk nature of the synchrotron powder X-ray probe, this indicates that fraction of vacancies on chalcogen atomic site, if any, is probably very small. On the other hand, synchrotron powder X-ray diffraction Rietveld refinement indicates vacancies on Fe atomic site in doped crystal alloys (Fig. S1f), consistent with TEM results [(Fig. 1a-j) main text]. Yet, attempts to refine Fe vacancy defect for FeSe and FeS also did not improve the fit beyond about 1 atomic %, i.e. for Fe_{1-y}Se and Fe_{1-y}S y=0.01(1). Therefore, in the text we use FeSe and FeS.

Note that, whereas we combined two different synthesis methods to tune disorder, crystals near x = 0.5 and x = 1 are created using the same hydrothermal crystal growth. FeS is a very good metal with low defect scattering.^{6,7} in contrast to crystals in the middle of the alloy series. Consequently, room temperature resistivity values for crystals for $0.4 \le x \le 0.8$ are much higher when compared to either x = 0 or x = 1 (Fig. S2). This implies that disorder is continuously tuned with x.

3. MAGNETIC SUSCEPTIBILITY

The superconducting T_c values inferred from the diamagnetic signal (Fig. S3) are consistent with those determined by resistivity. Both underdoped and overdoped samples show relatively sharp transitions in contrast to relatively broad in the range $(0.21 \le x \le 0.70)$. The onset of the diamagnetic signal is observed when the resistivity drops to zero. Close inspection shows that the transition starts to broaden when T_s is completely suppressed. With further S substitution samples exhibit wide transitions.

4. BLOCH-GRÜNEISEN MODEL FOR $\rho(T)$ FOR HIGH x

nematic state is dominated by electronic scattering (Fig. S4a).⁸ Nevertheless, $\rho(T)$ for $x \ge 0.4$ (Fig. S4b) is a MgB₂-like, suggesting phonon-related scattering. In the main text (Fig. 4) we fit resistivity of Fe_{1-y}Se_{0.52}S_{0.48} and FeS with a Bloch-Grüneisen curves^{9,10} $\rho(T) = \rho_0 + A\left(\frac{T}{\theta_D}\right)^5 \int_0^{\theta_D/T} \frac{x^5}{(e^x-1)(1-e^x)} dx$. Heat capacity at low temperature for FeS and Fe_{1-y}Se_{0.52}S_{0.48} is fitted with Debye model C/T = γ + β T²+ δ T⁴; values of electronic heat capacity $\gamma = 5.2$ (1) mJ·mol⁻¹·K⁻² and 6.2(3) mJ·mol⁻¹·K⁻² and of Debye temperature $\theta_D = 240(1)$ K and 208(1) K were obtained from fits in Fig. S4c,d, respectively using $\theta_D = (12\pi^4NR/5\beta)^{1/3}$ where N is the atomic number in the chemical formula and R is the universal gas constant. From the same fits values of prefactor A are 0.30(1) and 4.15(2)

Here we comment on the scattering mechanism. Resistivity in the

2

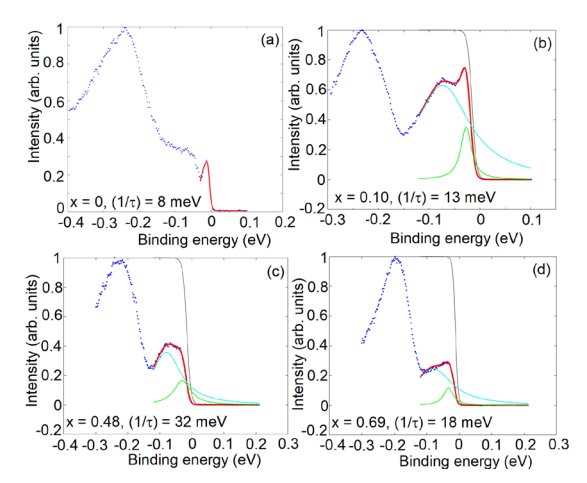


Fig. S5. Energy distribution curves and fitted Lorenzians for FeSe (a), $Fe_{1-y}Se_{0.9}S_{0.1}$ (b) and $Fe_{1-y}Se_{0.52}S_{0.48}$ (c) and $Fe_{1-y}Se_{0.31}S_{0.69}$ (d).

were obtained for FeS and FeSe_{0.52}S_{0.48}, respectively. A is related ^{11,12} to electron-phonon coupling constant λ via $A \sim \frac{\lambda}{\theta_D^4 \omega_p^2}$ where ω_p^2 is the plasma frequency. Given small changes in Debye temperature and typical $\lambda \sim (0.1$ - 0.3) in metals, large changes of A point to significant reduction of plasma frequency in doped samples. Since $\omega_p^2 \sim \frac{N_0 E_F}{m^*}$ in case for two-dimensional parabolic band ¹³ where N_θ is band density of states, E_F is Fermi energy and m^* is quasiparticle mass, this result could point to change of electronic correlations in doped samples.

In fact, according to our DFT+DMFT calculations for FeSe $_{0.5}S_{0.5}$ model (see also section 6 below), we found the average Fe-3d quasiparticle weight $Z_{\rm DMFT}$ = m/m* = 0.44, whereas in the case of FeS we obtained a larger quasiparticle weight of 0.52. This indicates an increase of electronic correlations upon replacing S by Se in FeS; also agrees with the change of γ in heat capacity fits. Further, as can be noticed in Fig. S4e, we observe a small suppression in the density of states, near the Fermi energy of FeSe $_{0.5}S_{0.5}$ in comparison to FeS.

Overall, these trends point out a reduction trend of the plasma frequency in for x=0.5 in comparison to x=1, which agrees with our experimental findings.

5. ARPES SCATTERING RATES

To measure the electronic structure, we took several momentum cuts along Γ -M direction using incoming photon energy hv = 120 eV and circular polarization. From the different cuts, we reconstruct the Fermi surface as shown in Figure S5. To examine the scattering rate, we measure the band dispersion along the high symmetry line Γ -M direction using a low incoming photon energy of hv = 25 eV to obtain high-resolution measurements both in energy and momentum. For each cut acquired from a sample with different x, we extract the energy distribution curve (EDC) at momentum k_F of the outer band defined as the peak at minimal binding energy with respect to the Fermi energy and have the larger k_F value. The EDCs were normalized to their high binding energy values and the background was removed by subtracting an EDC measured deep in the unoccupied region. To estimate the influence of S on the scattering rate, we have fitted the EDC to the two Lorentzians corresponding to the two bands. The width of the Lorentzian peak near the Fermi energy can be considered as a measure that tracks the evolution of the scattering rate with doping.

6. DFT+DMFT SCATTERING RATES

Our density functional theory plus dynamical mean field theory (DFT+DMFT) calculations were performed at the fully charge self-consistent level¹⁴ at 116 K. The DFT calculations were performed within Perdew-Burke-Ernzehof generalized gradient approximation (PBE-GGA) as implemented in WIEN2K.^{15,16} The DMFT effective impurity problem was solved using continuous time quantum Monte Carlo,¹⁷ within a Hubbard U = 5.0 eV and Hund's coupling J = 0.8 eV. In both FeSe and FeS near the Fermi energy around the Γ point the electronic states are composed by distinct mixtures of Fe 3*d* orbitals.¹⁸⁻²⁰ In addition, the average anion height above Fe plane relates to the hole pocket of d_{xy} orbital character.²¹ To investigate the degree of electronic correlations in the FeSe_{0.5}S_{0.5} we construct a model using a (2x2) supercell where we have an equal amount of Se and S atoms. From our DFT+DMFT calculations we evaluate the quasiparticle scattering rate at T = 116 K from the extrapolation of the imaginary-frequency self-energy to zero: $\Gamma = -Z_{\alpha}Im \sum_{\alpha}(i0^{+})$ where α is orbital index and Z_{α} is the quasiparticle weight.^{22,23}

The quasiparticle weight, in turn, is evaluated as $Z_{\alpha}^{-1} = \frac{\partial Im \sum_{\alpha} (i\omega)}{\partial \omega} \Big|_{\omega \to 0^+}$.

Table S1. DFT+DMFT d_{xy} scattering rates. Calculated scattering rates (in meV) are shown for unrelaxed (U) and relaxed (R) crystal structures of FeSe, FeSe_{0.5}S_{0.5}, and pure FeS.

Structure	FeSe	FeSe _{0.5} S _{0.5}	FeS
1/τ d _{xy} (meV) - U	5.6	1.9	1.2
$1/\tau d_{xy}$ (meV) - R	14.4	5.9	4.4
		2	

Table S2. DFT+DMFT orbital and site averaged scattering rates (meV) for FeSe_{0.5}S_{0.5}. Calculated scattering rates are shown in meV.

Fe site	d_{xy}	d_{xz}	d_{yz}	d_{z2}	d_{x2-y2}
Fe1	7.8	3.9	5.8	0.7	0.6
Fe2	3.6	3.7	4.1	0.4	0.4
Fe3	6.6	4.6	4.5	1.3	2.6
Fe4	5.6	2.8	4.5	0.3	1.5
Average	5.9	3.8	4.7	0.7	1.3

To investigate the effect of the alloying we considered the experimental lattice parameters. In unrelaxed structures (U) Fe-Ch (Ch = Se,S) the bond distances were constrained to the local experimental bond distances (Fe-Se = 2.395

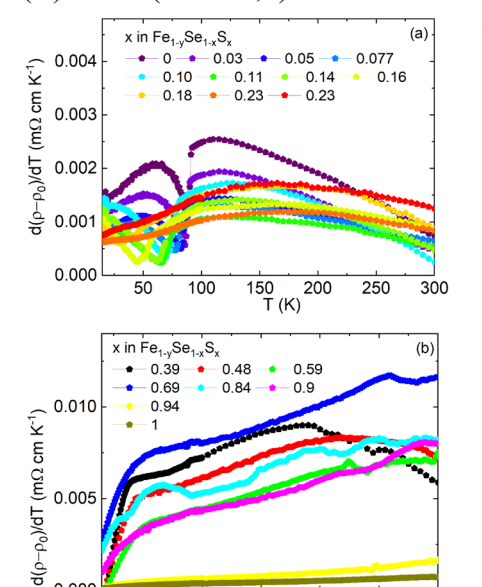


Fig. S6: Resistivity slope evaluated via temperature derivative of $[\rho(T)-\rho_0]$.

150

100

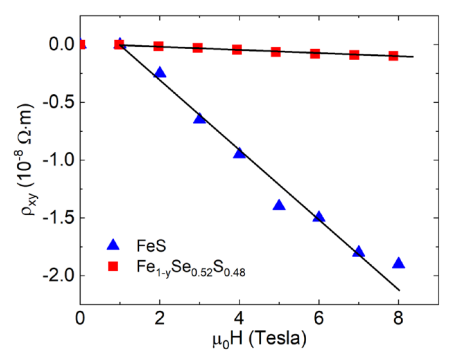


Fig. S7: Estimate of carrier density change between FeS and FeSe_{0.52}S_{0.48}.

Å and Fe-S = $2.265 \text{ Å})^{24,25}$ whereas after the structural relaxation (R) the distances between atoms are slightly increased (Fe-Se = 2.427 Å and Fe-S = 2.301 Å). For our FeSe_{0.5}S_{0.5} model we found largest scattering rates for the electronic states associated with Fe- d_{xy} orbitals. In Table S1 we display the obtained d_{xy} scattering rates for the pristine systems as well as for the alloy. The orbital and site averaged scattering rates for the latter are shown in Table S2.

From Tables S1 and S2 it is evident that d_{xy} scattering rates are very sensitive to Fe-Se and Fe-S bond lengths. The total scattering for FeSe_{0.5}S_{0.5}, obtained as the site and orbital average scattering rates, is around 3.3 meV (Table S2). On the other hand, the orbital averaged scattering rates for FeSe and FeS (relaxed structures) are 11.3 and 2.1 meV, respectively.

7. RESISTIVITY SLOPE AND CARRIER CONCENTRATION

Values of ρ_0 (Fig. 4e main text) were extracted from $\rho(T)$ for all x by linear extrapolation of low-temperature data. Derivative of temperature-dependent resistivity for all x is shown in Fig. S6. We note significant rise of resistivity slope $d[\rho(T)-\rho_0]/dT$ in the middle of the alloy series; values at 150 K are plotted in Fig. 4f main text. In the main text we note the large change of slope of resistivity curves when disorder is added in contrast to Matthiesen's rule. This is

also obvious when comparing FeS and samples near x=0.5 (Fig. S4a,b). It is also worth noting one more very clear feature of the data, at intermediate concentrations. Here we see substantial ρ_0 , but the T-dependent parts (Fig. S4a,b), i.e. $d[\rho(T)-\rho_0]/dT$ (Fig. S6) are quite similar for at all $0.48 \le x \le 0.9$. For example, curves x=0.9 and x=0.59 are almost parallel as if the validity of Matthiassen's rule is "restored" at these intermediate concentrations. Hence, when impurities in relatively good metals FeSe and FeS are added (S in FeSe and Se in FeS), additional scattering centers are produced but the nature of resulting scattering is x — dependent in a manner that is inconsistent with the standard picture of weak disorder effects. Our data indicate that the correlation effects are absent near FeS, but are activated as x is decreased from 0.9. This produces large temperature-dependent scattering that persists up to the room temperature. These effects can not be explained by the carrier concentration

reduction as x is reduced from 1; on the contrary carrier concentration is increased. Hall resistivity at T = 20 K (Fig. S7) of FeS is consistent with previously observed.²⁷ The slopes in Fig. S7 are equivalent to $R_H = 3 \cdot 10^{-9}$ m³/C and -1.39·10⁻¹⁰ which corresponds to -2.3·10²⁷ m⁻³ and -4.5·10²⁸ m⁻³ for FeS and FeSe_{0.52}S_{0.48}, respectively.

8. SUPPLEMENTARY REFERENCES

- 1. Hu, Rongwei; Lei, Hechang; Abeykoon, Milinda; Bozin, Emil S.; Billinge, Simon J. L.; Warren, J. B.; Siegrist, Theo, Petrovic, C.; Synthesis, crystal structure and magnetism of β-Fe_{1.00(2)}Se_{1.00(3)} single crystals. *Phys. Rev. B* **2011**, *83*, 224502.
- 2. Chareev, Dmitriy; Osadchii, Evgeniy; Kuzmicheva, Tatiana; Lin, Jiunn-Yuan; Kuzmichev, Svetoslav; Volkova, Olga; Vasiliev, Alexander; *Crystengcomm* **2013**, *15*, 1989-1993.
- 3. Wang, Aifeng; Milosavljevic, Ana; Abeykoon, A. M. Milinda, Ivanovski, Valentin; Du, Qianheng; Baum, Andreas; Stavitskii, Eli; Liu, Yu; Lazarevic, Nenad; Attenkofer, Klaus; Hackl, Rudi; Popovic, Zoran; Petrovic, Cedomir; Suppression of Superconductivity and Nematic Order in Fe_{1-y}Se_{1-x}S_x ($0 \le x \le 1$; $y \le 0.1$) Crystals by Anion Height Disorder. *Inorg. Chem.* **2022**, *61*, 11036-11045.
- 4. Borg, Christopher K. H.; Zhou, Xiuquan; Eckberg, Christopher; Campbell, Daniel J.; Saha, Shanta R.; Paglione, Johnpierre; Rodriguez Efrain E.; Strong anisotropy in nearly ideal tetrahedral superconducting FeS single crystals. *Phys. Rev. B* **2016**, *93*, 094522.
- 5. Toby, B. H.; Von Dreele, R. B; GSAS-II: the genesis of a modern opne-source all purpose crystallography software package. *J. Appl. Crystallogr.* **2013**, *46*, 544-549.
- 6. Terashima, Taichi; Kikugawa, Naoki; Lin, Hai; Zhu, Xiyu; Wen, Hai-Hu; Nomoto, Takuya; Suzuki, Katsuhiro; Ikeda, Hiroaki; Uji, Shinya; Upper critical field and quantum oscillations in tetragonal superconducting FeS. *Phys. Rev. B* **2016**, *94*, 100503(R).
- 7. Terashima, Taichi; Kikugawa, Naoki; Kiswandhi, Andhika; Choi, Eun-Sang; Brooks, James S.; Kasahara, Shigeru; Watashige, Tatsuya; Ikeda, Hiroaki; Shibauchi, Takasada; Matsuda, Yuji; Wolf, Thomas; Böhmer, Anna E.; Hardy, Frédéric; Meingast, Chrisoph; v. Löhneysen, Hilbert; Suzuki, Michi-To; Arita, Ryotaro, Uji, Shinya; Anomalous Fermi surface in FeSe seen by Shubnikov-de Haas oscillation measurements. *Phys. Rev. B* **2014**, *90*, 144517.
- 8. Licciardello, S.; Buhot, J.; Lu, J.; Ayres, J.; Kasahara, S.; Matsuda, Y.; Shibauchi, T. Hussey, N. E.; Electrical resistivity across a nematic quantum critical point. *Nature* **2019**, *567*, 213-217.
- 9. M. Ziman, Electronis and Phonons. Clarendon, Oxford 1962.
- 10. Kim, Kijoon H. P.; Choi Jae-Hyuk; Jung, C. U.; Chowdhury, P.; Lee, Hyun-Sook; Park, Min-Seok; Kim, Heon-Jung; Kim, J. Y.; Du, Zhonglian; Choi, Eun-Mi; Kim, Mun-Seog; Kang, W. N.; Lee, Sung-Ik; Sung, Gun Yong; Lee, Jeong, Yong; Superconducting properties of well-shaped MgB₂ single crystals. *Phys. Rev. B* **2002**, *65*, 100510.
- 11. Santos-Cottin, David; Gauzzi, Andrea; Verseils, Marine; Baptiste, Benoit; Feve, Gwendal; Freulon, Vincent; Plaçais, Casula, Michele; Klein, Yannick; Anomalous metallic state in quasitwo-dimensional BaNiS₂. *Phys. Rev. B* **2016**, *93*, 125120.
- 12. Takeya, Hiroyuki; Elmassalami, Mohammed; Linear magnetoresistivity in the ternary AM_2B_2 and $A_3Rh_8B_6$ phases (A = Ca, Sr; M = Rh, Ir). Phys. Rev. B **2011**, 84, 064408.
- 13. Di Castro, D.; Ortolani, M.; Cappelluti, E.; Schade, U.; Zhigadlo, N. D.; Karpinski, J.; Infrared properties of Mg_{1-x}Al_x(B_{1-y}C_y)₂ single crystals in the normal and superconducting state. *Phys. Rev. B* **2006**, *73*, 174509.
- 14. Haule, Kristjan; Yee, Chuck-Hou; Kim, Kyoo; Dynamical mean-field theory within the full-potential methods: Electronic structure of CeIrIn₅, CeCoIn₅ and CeRhIn₅. *Phys. Rev. B* **2010**, *81*, 195107.
- 15. Perdew, John P.; Burke, Kieron; Ernzerhof, Matthias; Phys. Rev. Lett. 1996, 77, 3865-3868.
- 16. P. Blaha, K. P. Schwarz and G. K. H. Madsen, WIEN2K, An Augmented Plane Wave + Local Orbitals Program for Calculating Crystal Properties (Karlheinz Schwarz, Techn. Universität Wien, Austria, 2001).
- 17. Haule, Kristjan; Quantum Monte Carlo impurity solver for cluster dynamical mean-field theory and electronic structure calculations with adjustable cluster base. *Phys. Rev. B* **2007**, *75*, 155113.
- 18. Miao, J.; Niu, X. H.; Xu, D. F.; Yao, Q.; Chen, Y.; Ying, T. P.; Li, S. Y.; Fang, Y. F.; Zhang, J.

- C.; Ideta, S.; Tanaka, K.; Xie, B. P.; Feng, D. L.; Chen, Fei; Electronic structure of FeS. *Phys. Rev. B* **2017**, *95*, 205127.
- 19. Kostin, A.; Sprau, P. O.; Kreisel, A.; Chong, Yi Xue; Böhmer, A. E.; Canfield, P. C.; Hirshfeld, P. J.; Anderson, B. M.; Davis, J. C. Séamus; Imaging orbital-selective quasiparticles in the Hund's metal state of FeSe. Nat. Mater. **2018**, 17, 869-874.
- 20. Yi, M.; Pfau, H.; Zhang, Y.; He, Y.; Wu, H.; Chen, T.; Ye, Z. R.; Hashimoto, M.; Yu. R.; Si, Q.; Lee, D.-H.; Dai, Pengcheng; Shen, Z.-X.; Lu, D. H.; Birgenau, R. J.; Nematic Energy Scale and the Missing Electron Pocket in FeSe. Phys. Rev. X 2019, 9, 041049.
- 21. Sato, Masatoshi; Tanaka, Yukio; Yada, Keiji; Yokohama, Takehito; Topology of Andreev bound states with flat dispersion. Phys. Rev. B **2011**, *79*, 224511.
- 22. Zhang, Peng; Cohen, R. E.; Haule, K.; Effects of electron correlations on transport properties of iron at Earth's core conditions. Nature **2015**, *517*, 605-607.
- 23. Pourovskii, L. V.; Miyake, T.; Simak, S. I.; Ruban, A. V.; Dubrovinsky, L.; Abrikosov, I. A.; Electronic properties and magnetism of iron at the Earth's inner core conditions. Phys. Rev. B **2013**, *87*, 115130.
- 24. Pomjakushina, E.; Conder, K.; Pomjakushin, V.; Bendele, M.; Khasanov, R.; Synthesis, crystal structure and chemical stability of the superconductor FeSe_{1-x}. Phys. Rev. B **2009**, *80*, 024517.
- 25. Pachmayr, U.; Fehn, N.; Johrendt, D.; Structural transition and superconductivity in hydrothermally synthesized FeX (X = S, Se). Chem. Comm. **2016**, *52*, 194-197.
- 26. Reiss, Pascal; Graf, David; Haghighirad, Amir A.; Knafo, William; Drigo, Loïc; Bristow, Matthew; Schofield, Andrew J.; Coldea, Amalia I.; Quenched nematic criticality and two superconducting domes in an iron-based superconductor. *Nature Physics* **2020**, *16*, 89-95.
- 27. Lin, Hai; Li, Yufeng; Deng, Qiang; Xing, Jie; Liu, Jianzhong; Zhu, Xiyu; Yang, Huan; Wen, Hai-Hu; Multiband superconductivity and large anisotropy in FeS crystals. *Phys. Rev. B* **2016**, *93*, 144505.